Stripping and excitation in collisions between p and $He^+(n \leqslant 3)$ calculated by a quantum time-dependent approach with semiclassical trajectories

Vladimir S. Melezhik,[1,*] James S. Cohen,[2] and Chi-Yu Hu[1]
[1]*Department of Physics and Astronomy, California State University at Long Beach, Long Beach, California 90840, USA*
[2]*Theoretical Division, Los Alamos National Laboratory, Los Alamos, New Mexico 87545, USA*
(Received 13 June 2003; published 19 March 2004)

Stripping and excitation cross sections are calculated, using a time-dependent discrete-variable approach, for collisions of protons with energies from 0.5 keV to 2 MeV with He^+ initially in the 1*s*, 2*s*, 2*p*, 3*s*, 3*p*, and 3*d* states. This quantum-semiclassical approach takes trajectory curvature into account. The spatial and temporal convergence properties of the method are analyzed for the ground and higher states. The results are in good agreement with existing accurate calculations and experimental cross sections, available for $E_p \geqslant 3.73$ keV. Results are also obtained for lower-energy collisions where the cross sections are still significant but trajectory curvature is important.

DOI: 10.1103/PhysRevA.69.032709 PACS number(s): 34.50.Fa, 34.10.+x

I. INTRODUCTION

The collision of a hydrogenlike ion with a proton of energy sufficiently high to break up the ion is an example of the fundamental three-body problem with Coulomb interaction. It is also important in fusion plasmas [1]. These processes have been extensively investigated with various theoretical approaches, including the Born and distorted-wave approximations [2,3], the classical-trajectory Monte Carlo method [4], the continuum-distorted-wave–eikonal-initial-state method [2], coupled-channel basis-set expansions with *a priori* assumed (usually straight-line and well-justified) trajectory [3,5,6], hidden adiabatic energy crossings in the complex plane [7,8], and solution of the time-dependent Schrödinger equation with classical trajectory for the projectile [9], as well as experimentally [10–13]. The high-energy regime seems to be well understood. However, in the region of medium and low energies ($E < 100$ keV) there are still significant differences between the various theoretical calculations. Also, the existing computations have been performed only for the ground state of the ion and, in some cases, low-lying excited *s* states.

Most accurate schemes for treating the ionization and electron transfer in this region have been based on the impact-parameter approach with straight-line trajectories for the relative target-projectile motion. Trajectory curvature effects, which become important at low collision energies [14,15], have not been well studied previously.

II. METHOD

The present method was originally developed [16] for treating nonsudden behavior in the sticking problem following muon-catalyzed fusion [17]. In subsequent work, it has been applied to high-harmonics generation by a hydrogen atom in an elliptically polarized laser field [18,19], excitations of muonic helium by magnetic fields [20], ionization of ions moving in magnetic fields [21], and breakup of halo nuclei [22,23]. In treating the different quantum dynamics, the method has been found to be highly efficient and flexible.

We present here the computational scheme with results for the reactions

$$(He^+)_{n_i l_i} + p \rightarrow e + He^{++} + p, \tag{1}$$

$$(He^+)_{n_i l_i} + p \rightarrow (H)_{n_f} + He^{++}, \tag{2}$$

and

$$(He^+)_{n_i l_i m_i} + p \rightarrow (He^+)_{n_f l_f m_f} + p. \tag{3}$$

These transitions are affected by the time-dependent Coulomb field between the He^+ and proton.

A. General scheme

The collisions are described by solutions of the time-dependent Schrödinger equation

$$i\hbar \frac{\partial}{\partial t}\psi(\mathbf{r},t) = [H_0(\mathbf{r}) + V(\mathbf{r},\mathbf{R}(t))]\psi(\mathbf{r},t), \tag{4}$$

where the wave packet $\psi(\mathbf{r},t)$ corresponds to the relative motion of the electron and the helium nucleus. In this expression,

$$H_0 = -\frac{1}{2\mu}\nabla_{\mathbf{r}}^2 - \frac{2}{r} \tag{5}$$

is the internal Hamiltonian of He^+ with reduced mass $\mu = m_e m_{\mathrm{He}}/M$, where m_e and m_{He} are the masses of the electron and helium nucleus, respectively, and $M = m_e + m_{\mathrm{He}}$. The interaction of the projectile p with the target He^+ is given by

*Permanent address: Joint Institute for Nuclear Research, Dubna, Moscow Region 141980, Russian Federation.

$$V(\boldsymbol{r},t) = \frac{2}{|\boldsymbol{R}(t) + m_e\boldsymbol{r}/M|} - \frac{1}{|\boldsymbol{R}(t) - m_{\mathrm{He}}\boldsymbol{r}/M|}, \tag{6}$$

where $\boldsymbol{R}(t)$ is the relative coordinate between the projectile and center of mass of the target. The Schrödinger equation (4) is integrated simultaneously with the classical Hamilton equations [20,21]

$$\frac{d}{dt}\boldsymbol{P}(t) = -\frac{\partial}{\partial \boldsymbol{R}} H_{cl}(\boldsymbol{P}(t),\boldsymbol{R}(t)), \tag{7a}$$

$$\frac{d}{dt}\boldsymbol{R}(t) = \frac{\partial}{\partial \boldsymbol{P}} H_{cl}(P(t),\boldsymbol{R}(t)), \tag{7b}$$

where

$$H_{cl}(\boldsymbol{P},\boldsymbol{R}) = \frac{1}{2M_0}\boldsymbol{P}^2 + H_0(\boldsymbol{p},\boldsymbol{r}) + \langle \psi(\boldsymbol{r},t)|V(\boldsymbol{r},\boldsymbol{R})|\psi(\boldsymbol{r},t)\rangle, \tag{7c}$$

with $M_0 = m_p M/(m_p+M)$. The computational scheme includes the coupling between the electron and projectile variables and conserves the total energy of the system.

The key idea to simultaneously treat quantum and classical degrees of freedom goes back to Refs. [24,25] where it was applied to the collisional dynamics of molecular processes. Note also the similar self-consistent classical-quantum treatment of muon capture by the hydrogen atoms [26] and recent time-dependent calculations of the atomic hydrogen ionization by antiproton impact [27].

We use the global basis on the subspace grid (θ_i, ϕ_i) for the angular variables of the electron coordinate $\boldsymbol{r}$ in the spirit of the discrete-variable technique. This yields a diagonal representation for the interaction $V(r, \theta_i, \phi_i, t)$ between the projectile and target. As a consequence, the problem is reduced to the Schrödinger-type time-dependent radial equations coupled only through the nondiagonal angular part of the kinetic energy operator. This equation is propagated using a split-operator method, which permits fast diagonalization of the remaining nondiagonal part [19,22]. For discretizing with respect to the radial variable r, a sixth-order (seven-point) finite-difference approximation on a quasiuniform grid is used. The scheme is unconditionally stable, maintains unitarity, and has the same order of accuracy as the conventional Crank-Nickolson algorithm. It allows a full three-dimensional (3D) quantal treatment of the electronic motion during the collisions. The only additional simplification is the use of the classical approximation for the relative projectile-target trajectory $\boldsymbol{R}(t)$ [determined by Eqs. (7)], which is physically well justified for the range of the velocities considered in the present work.

We note a principal advantage of our scheme as compared with the previous classical-quantum approaches [9,24–27]. In previous calculations, the Schrödinger equation was solved with an expansion in spherical harmonics. Therefore it requires analytical treatment of the angular part of the necessary integrals. In such a scheme, the matrix elements H_{cl} in Eq. (7c) can be calculated only with a multipole expansion of the time-dependent potential (6) [24,25], which in some kinematical regions can be a challenging computational problem. Our approach is free from this drawback since we use a discrete representation for the electronic angular variables. In our representation the matrix (6) is diagonal, and the diagonal elements are simply the values of the potential $V(\boldsymbol{r},t)$ at the angular grid points.

In the next two subsections, we give a more detailed consideration of solving the Schrödinger equation (4) and describing the collisional dynamics.

B. Angular-subspace discretization

We seek a solution $\psi(\boldsymbol{r},t)$, in spherical coordinates $(r,\Omega) \equiv (r,\theta,\phi)$, as an expansion

$$\psi(\boldsymbol{r},t) = \frac{1}{r}\sum_{\nu j}^{N} Y_\nu(\Omega)(Y^{-1})_{\nu j}\psi_j(r,t) \tag{8}$$

over the two-dimensional basis

$$Y_\nu(\Omega) = \sum_{\nu'} C_{lm}^{l'm'} P_{l'}^{m'}(\theta) e^{im'\phi}. \tag{9}$$

In this basis, $C_{lm}^{l'm'} = \delta_{ll'}\delta_{mm'}$, in general, and thus $Y_\nu(\Omega)$ coincides with a usual spherical harmonic with a few possible exceptions for high ν as explained below after Eq. (11). The symbol ν represents $\{l,m\}$ and the sum over ν is equivalent to the double sum

$$\sum_{\nu=1}^{N} = \sum_{l=0}^{\sqrt{N}-1}\sum_{m=-l}^{l}. \tag{10}$$

In previous works [18–23] another scheme

$$\sum_{\nu=1}^{N} = \sum_{m=-(\sqrt{N}-1)/2}^{(\sqrt{N}-1)/2}\sum_{l=|m|}^{|m|+\sqrt{N}-1}$$

of constructing the angular basis was applied, which sometimes gives faster convergence but omits high values of m for $l > \sqrt{N}-1$. This peculiarity becomes important in the present computations as we analyze transitions to high n_f in collisional excitations (3).

The basis (9) is associated with a mesh. For the θ variable, the $\sqrt{N}$ mesh points θ_{j_θ} correspond to the zeros of the Legendre polynomial $P_{\sqrt{N}}(\cos\theta_{j_\theta})$. For the ϕ variable, the $\sqrt{N}$ mesh points are chosen as $\phi_{j_\phi} = \pi(2j_\phi - 1)/\sqrt{N}$. The total number N of grid points $\Omega_j = (\theta_{j_\theta}, \phi_{j_\phi})$ is equal to the number of basis functions in expansion (8) [19,22]. With this mesh are associated N weights λ_j, which are the standard Gauss-Legendre weights multiplied by $2\pi/\sqrt{N}$. The $(Y^{-1})_{\nu j}$ are the elements of the $N\times N$ matrix Y^{-1} inverse to the matrix with elements $Y_{j\nu} = Y_\nu(\Omega_j)$ defined at the grid points Ω_j. The polynomials $Y_\nu(\Omega)$ are chosen in such a way, Eq. (9), that one has exactly

$$\int Y_\nu^*(\Omega)Y_{\nu'}(\Omega)d\Omega = \sum_j \lambda_j Y_{\nu j}^* Y_{\nu' j} = \delta_{\nu\nu'} \tag{11}$$

for all ν and $\nu' \leqslant N$. For most ν and ν', property (11) is automatically satisfied because the basis functions $Y_\nu(\Omega)$ are

orthogonal and the Gaussian quadrature is exact. For these ν the coefficients $C_{lm}^{l'm'}=\delta_{ll}\delta_{mm}$ in Eq. (9). However, in a few cases involving the highest l and m values, some polynomials Y_l^m have to be specially made orthogonal in the sense of the Gaussian quadrature ($C_{lm}^{l'm'}\neq\delta_{ll}\delta_{mm}$ for these specific l and m). With this choice, the matrix $\lambda_j^{1/2}Y_{j\nu}$ is orthogonal.

The radial components $\psi_j(r,t)$ correspond to $\psi(r,\Omega_j,t)$, which is a complex function. We introduce the N-component vector $\psi(r,t)=\{\lambda_j^{1/2}\psi_j(r,t)\}$. With respect to the unknown coefficients in expansion (8), the problem is then reduced to a system of Schrödinger-type equations

$$i\hbar\frac{\partial}{\partial t}\psi(r,t)=[\hat{H}_0(r)+\hat{V}(r,t)]\psi(r,t). \tag{12}$$

In this system, $\hat{H}_0(r)$ and $\hat{V}(r,t)$ are $N\times N$ matrix operators representing H_0 and V [Eqs. (5) and (6)] on the grid. The elements of $\hat{H}_0(r)$ are defined by

$$H_{0kj}(r)=-\left(\frac{1}{2\mu}\frac{\partial^2}{\partial r^2}+\frac{2}{r}\right)\delta_{kj}+\frac{1}{2\mu r^2}(\lambda_k\lambda_j)^{-1/2}\times\sum_{\nu=\{l,m\}}^{N}(Y^{-1})_{k\nu}l(l+1)(Y^{-1})_{\nu j}. \tag{13}$$

The elements of $\hat{V}(r,t)$ are

$$V_{kj}(r,t)=V(r,\Omega_k,t)\,\delta_{kj}. \tag{14}$$

The values of the wave function $\psi(\mathbf{r},t)$ at the grid points of the angular space $\psi(r,\Omega_j,t)$ are utilized in the spirit of the discrete-variable representation (DVR) [28] or Lagrange-mesh methods [29]. It drastically simplifies the calculations as compared with the usual partial-wave analysis. In fact, the time-dependent Coulomb operator defined in Eq. (6) is a diagonal matrix (14) in such a representation, and the diagonal elements $V(r,\Omega_k,t)$ are simply the values of the potential $V(\mathbf{r},t)$ at the angular grid points. It does not require the multipole expansion used in other approaches [9,24–27].

Note that we have replaced in Eq. (13) the angular matrix elements $\langle Y_\nu|L^2|Y_{\nu'}\rangle$ by $l(l+1)\delta_{ll'}\delta_{mm'}$. This is, however, not exact for some high l and m for fixed N. But the approximation is consistent with the accuracy of the Gaussian approximation employed for the matrix elements $\langle Y_\nu|\hat{V}|Y_{\nu'}\rangle$ of the interaction in Eq. (14).

The rapid convergence of the expansion (8) has been demonstrated in problems describing different quantum dynamics [18–23].

C. Computational scheme

Another attractive feature of the present approach is that the only nondiagonal part of the Hamiltonian in Eq. (12)—the angular part of the kinetic energy operator [see Eq. (13)]—can be diagonalized by the simple unitary transformation $S_{k\nu}=\lambda_k^{1/2}Y_{k\nu}$ [19,22]. This property has been exploited for developing an economical algorithm with a computational time proportional to the number N of unknowns in the system of equations (12) [19]. The component-by-component split-operator method [30] has been applied for the propagation in time $t_n\rightarrow t_{n+1}=t_n+\Delta t$ as

$$\psi(r,t_n+\Delta t)=(1+\tfrac{1}{2}i\Delta t\hat{V})^{-1}(1-\tfrac{1}{2}i\Delta t\hat{V})(1+\tfrac{1}{2}i\Delta t\hat{H}_0)^{-1}\times(1-\tfrac{1}{2}i\Delta t\hat{H}_0)\psi(r,t_n). \tag{15}$$

Thus the problem is split up into two steps involving the intermediate time $t_n+\frac{1}{2}\Delta t$.

At the initial step, the vector function $\psi(r,t_n+\frac{1}{2}\Delta t)$ is evaluated from the known vector function $\psi(r,t_n)$ using the system of N differential equations

$$[1+\tfrac{1}{2}i\Delta t\hat{S}\hat{H}_0(r)\hat{S}^\dagger]\overline{\psi}(r,t_n+\tfrac{1}{2}\Delta t)=[1-\tfrac{1}{2}i\Delta t\hat{S}\hat{H}_0(r)\hat{S}^\dagger]\overline{\psi}(r,t_n), \tag{16}$$

where

$$\overline{\psi}(r,t_n)=\hat{S}\psi(r,t_n). \tag{17}$$

The system of equations (16) is uncoupled since

$$(\hat{S}\hat{H}_0\hat{S}^\dagger)_{\nu\nu'}=\left[-\frac{1}{2\mu}\frac{\partial^2}{\partial r^2}-\frac{2}{r}+\frac{1}{2\mu r^2}l(l+1)\right]\delta_{\nu\nu'}, \tag{18}$$

where $\nu=\{l,m\}$. It is solved with the boundary conditions

$$\overline{\psi}(0,t_n+\tfrac{1}{2}\Delta t)=\overline{\psi}(r_m,t_n+\tfrac{1}{2}\Delta t)=0,\text{for } r_m\rightarrow\infty. \tag{19}$$

Then the wave function at time $t_n+\frac{1}{2}\Delta t$ is obtained as

$$\psi(r,t_n+\tfrac{1}{2}\Delta t)=\hat{S}^\dagger\overline{\psi}(r,t_n+\tfrac{1}{2}\Delta t). \tag{20}$$

The most time-consuming part in performing the initial step $t_n\rightarrow t_n+\frac{1}{2}\Delta t$ [Eqs. (16)–(20)]—namely, solving the boundary-value problem (16) and (19)—demands only N computational operations. Moreover, the $\hat{S}$ transformation is independent of t and r, and, as a consequence, the matrix $S_{k\nu}=\lambda_k^{1/2}Y_\nu(\Omega_k)$ has to be evaluated only once.

At the second step, the system of N uncoupled algebraic equations

$$[1+\tfrac{1}{2}i\Delta t\hat{V}(r,t_n)]\psi(r,t_n+\Delta t)=[1-\tfrac{1}{2}i\Delta t\hat{V}(r,t_n)]\psi(r,t_n+\tfrac{1}{2}\Delta t), \tag{21}$$

with the diagonal matrix $\hat{V}(r,t_n)$ defined in Eq. (14), is solved. Applying the split-operator method (15)–(21) to Eq. (12) demands that the two-dimensional basis $Y_\nu(\Omega)$, used in Eq. (8), be orthogonal on the grid Ω_k. It was shown in Ref. [19] that, because of the simplicity of the diagonalization procedure for the $\hat{H}_0(r)$ operator, the computational time for solving Eqs. (16)–(21) is approximately proportional to N as long as the computation time in Eqs. (17) and (20) is negligible with respect to the time for solving Eqs. (16) and (21); this is the case as long as N is not too large.

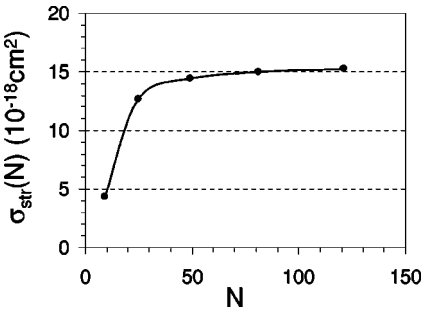

FIG. 1. The calculated cross section for the stripping from the ground state $He^+(1s)$ in $p+He^+$ collisions at $E_p=200$ keV as a function of the number N of the basis functions in the expansion (8).

III. RESULTS

In this approach, the stripping [including ionization (1) and electron transfer (2)] cross section $\sigma_{str}(n_i)$ and the excitation cross sections $\sigma_{ex}(n_i,n_f)$ are obtained by

$$\sigma_{str}(n_i) = 2\pi \int_0^\infty P_{str}(n_i) b db \tag{22a}$$

and

$$\sigma_{ex}(n_i,n_f) = 2\pi \int_0^\infty P_{ex}(n_i,n_f) b db. \tag{22b}$$

Here the stripping and excitation probabilities, $P_{str}(n_i)$ and $P_{ex}(n_i,n_f)$, are calculated according to

$$P_{str}(n_i) = 1 - \sum_{n_f=1}^{\infty} P_{ex}(n_i,n_f), \tag{23}$$

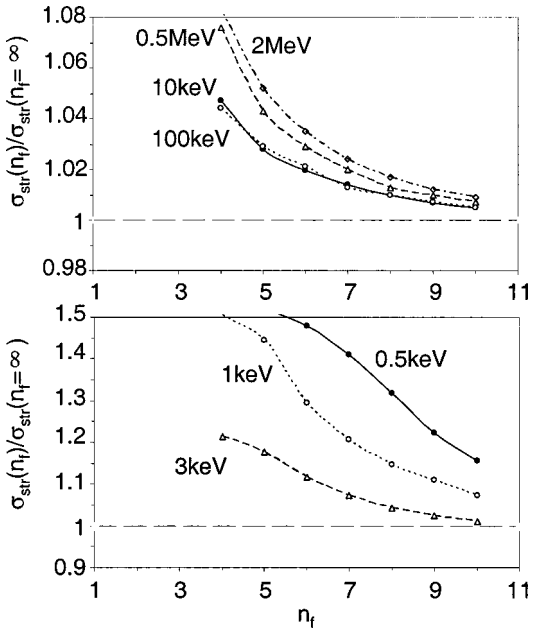

FIG. 2. Convergence of the calculated cross sections for the stripping from the ground state $He^+(1s)$ in $p+He^+$ collisions for a few proton energies as a function of n_f in Eq. (23).

$$P_{ex}(n_i,n_f) = \sum_{l_f=1}^{n_f-1} \sum_{m_f=-l_f}^{l_f} W_{l_i m_i} \left| \langle \phi_{n_f l_f m_f}(\mathbf{r}) | \psi^{(n_i l_i m_i)}(\mathbf{r}, t_{out} \to \infty) \rangle \right|^2, \tag{24}$$

assuming the electron to be initially (at $t_{in}=-T$) in the bound state $\phi_{n_i l_i m_i}$ of the helium ion with probability $W_{l_i m_i}$ and using wave-packet dynamics at large t ($t_{out}=T$). Since the problem

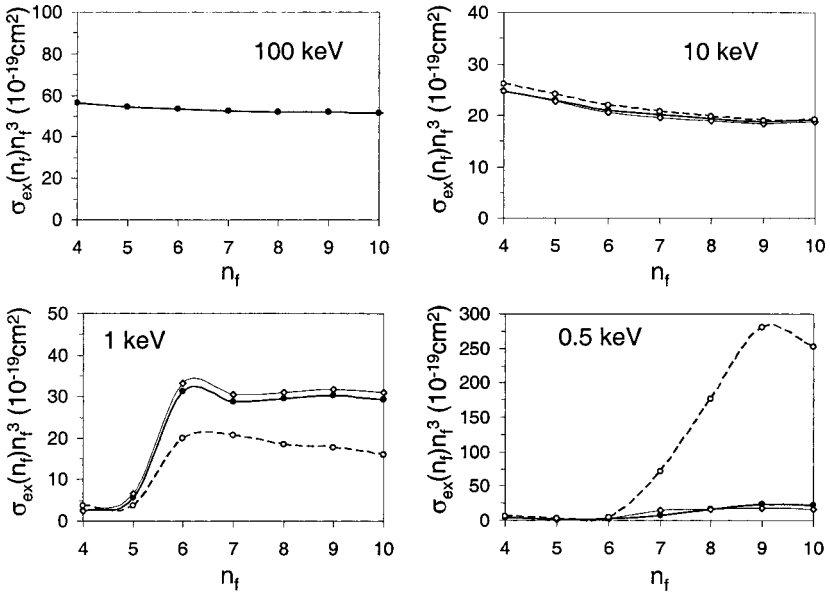

FIG. 3. The dependence of the calculated excitation cross sections on n_f in the region of large n_f for the transition from the ground state $n_i=1$ to excited states n_f. Solid curves, the results obtained by solving simultaneously the quantum-semiclassical system of equations (4)–(7); thin-solid and dashed curves, the results obtained by solving the Schrödinger equation (4) with Coulomb and straight-line trajectories, respectively.

TABLE I. Stripping cross sections $\sigma_{str}(n_i,l_i)$ (in units of 10^{-18} cm^2). The energies are the laboratory energies of the proton projectile.

n_il_i	0.5 keV	1 keV	10 keV	100 keV	200 keV	500 keV	1000 keV	2000 keV
1*s*	0.0287	0.0902	1.003	25.74	15.56	7.21	4.02	2.22
2*s*			602.7	111.5	60.6	27.17	14.78	7.94
2*p*			580.0	134.4	69.5	29.65	15.60	8.13
3*s*			1667	223	123.5	54.1	28.4	14.6
3*p*			1718	245	131.5	56.6	29.4	15.1
3*d*			2280	275	124.2	59.7	30.4	15.4

has azimuthal symmetry in the direction of the initial projectile momentum, it is natural to separate the Φ variable and parametrize the two remaining coordinates for the relative target-projectile motion with the impact parameter b. We consider the relative target-projectile motion in the plane Y-Z with the position of the target at the origin of the frame. The initial velocity $\boldsymbol{v}$ of the projectile is directed along the Z axis and the initial relative coordinates are defined as $Z(t_{in})=vt_{in}$ and $Y(t_{in})=b$ ($t_{in}=-T$). It is important to start computations at a sufficiently large initial distance $R(t_{in})$ between the target and projectile where the effect of the interaction potential (6) is negligible. This is achieved by choosing sufficiently large T. With such a parametrization, the nearest approach of the projectile and target occurs close to the time $t=0$. At the final point t_{out}, it is supposed that the projectile is already beyond the region of interaction, and one can use the calculated wave packet $\psi^{(n_il_im_i)}(\boldsymbol{r},T)$ for extracting the scattering parameters by formulas (22)–(24).

A. Convergence of the computational scheme

We have performed calculations of stripping, Eqs. (1) and (2), and excitation, Eq. (3), from the low bound states ($n_i=1,2,3$) of the helium ions for proton collision energies from 0.5 keV to 2 MeV for $n_i=1$ and for proton collision energies from 10 keV to 2 MeV for $n_i=2$ and 3.

For discretizing with respect to the radial variable r, a sixth-order (seven-point) finite-difference approximation on a quasiuniform grid has been used on the interval $r\in[0,r_m]$. This grid has been realized by the mapping $r\rightarrow x$ of the initial interval onto $x\in[0,1]$ by the formula $r=r_m(e^{6x}-1)/(e^6-1)$ [18]. The boundary of integration was chosen rather far at $r_m=100$ a.u. to prevent possible distortion of the spreading wave packet by the edge of the radial grid.

The calculations have been performed on the three-dimensional grids $\{r_i,\theta_j,\phi_j\}_{i,j=1,1}^{N_r,N}$ with up to $N=N_\theta\times N_\phi=13\times13=169$ angular and $N_r=2\times10^3$ radial grid points. Note that in this approach the number of angular grid points, N, is equal to the number of angular basis functions $Y_\nu(\hat{\mathbf{r}}_j)$ used for the expansion of the three-dimensional wave function (8). The steps of integration over the time variable were chosen as $\Delta t=0.05$–0.025 a.u. and the boundary of integration varied in the limits $T=10$–380 a.u., depending on the initial proton energy. On such a grid we were able to reproduce the binding energies of $(He^+)_{n_i}$ and the norms $\langle\psi(\mathbf{r},t_{in})|\psi(\mathbf{r},t_{in})\rangle=1$ for all initial n_i up to $n_i=7$ within eight significant digits. For all states from the shell $n_i=8$ the accuracy is better than 2×10^{-5}, for $n_i=9$ it is better than 3×10^{-3}, and for the state $n_i=10, l_i=m_i=0$ the accuracy is about 10^{-1} but improving with increasing l_i and m_i up to 4×10^{-4} at $n_i=10, l_i=m_i=9$.

TABLE II. Excitation cross sections $\sigma_{ex}(n_i,n_f)$ for the 1*s* initial state (in units of 10^{-18} cm^2). These cross sections are summed over final quantum numbers l_f and m_f.

E_p	0.5 keV	1 keV	10 keV	100 keV	200 keV	500 keV	1000 keV	2000 keV
$n_f=2$	0.06215	0.09247	1.181	10.39	8.696	5.626	3.653	2.248
$n_f=3$	0.02908	0.02719	0.1472	2.285	1.742	1.056	0.6650	0.4008
$n_f=4$	0.00591	0.00393	0.03869	0.8836	0.6555	0.3875	0.2415	0.1445
$n_f=5$	0.00173	0.00454	0.01838	0.4348	0.3196	0.1868	0.1158	0.06907
$n_f=6$	0.00107	0.01452	0.00969	0.2466	0.1802	0.1047	0.06477	0.03855
$n_f=7$	0.00234	0.00839	0.00588	0.1535	0.1118	0.06470	0.03996	0.02376
$n_f=8$	0.00308	0.00577	0.00380	0.1022	0.08482	0.04728	0.02918	0.01534
$n_f=9$	0.00323	0.00416	0.00258	0.07131	0.05174	0.02982	0.01839	0.01092
$n_f=10$	0.00226	0.00293	0.00192	0.05179	0.03754	0.02161	0.01332	0.00791
n_f: $11-\infty$	0.0102	0.0133	0.0087	0.2343	0.1699	0.0978	0.0603	0.0358

TABLE III. Excitation and deexcitation cross sections $\sigma_{ex}(n_i,n_f)$ for the 2*s* initial state (in units of 10^{-18} cm^2).

E_p	10 keV	100 keV	200 keV	500 keV	1000 keV	2000 keV
$n_f=1$	0.8193	2.552	1.239	0.4785	0.2321	0.1144
$n_f=3$	176.4	202.9	127.5	60.91	32.69	16.93
$n_f=4$	53.82	38.24	23.80	11.64	6.406	3.391
$n_f=5$	34.03	14.49	8.907	4.369	2.425	1.296
$n_f=6$	23.03	7.241	4.417	2.165	1.206	0.6473
$n_f=7$	16.72	4.197	2.547	1.247	0.6957	0.3744
$n_f=8$	11.77	2.695	1.631	0.7980	0.4455	0.2400
$n_f=9$	8.67	1.811	1.0903	0.5342	0.2984	0.1609
$n_f=10$	6.48	1.289	0.7765	0.3792	0.2119	0.1144
n_f: $11-\infty$	29.33	5.80	3.51	1.72	0.96	0.52

The accuracy of calculated cross sections (22) was estimated by comparing the results obtained on a sequence of converging grids with successively increasing numbers of grid points. The convergence with respect to the impact parameter *b* was also tested. Figure 1 illustrates the accuracy of the computational scheme by the convergence with respect to *N*. Such tests have permitted us to fix *N* at 121 for all the computations. By analogous numerical analyses we chose $N_r=1000$, $r_m=100$, and $b_m=10$. The resulting accuracy is of the order of 1% or better for proton energies greater than 10 keV. At lower energies the calculations performed on the chosen grids are slightly less accurate.

B. Extrapolation to higher n_f

Another important feature of the computational scheme is the procedure of extracting the stripping component from the wave packet in the final state (at t_{out}) by projection on the bound states n_f of the He ion. We have checked the accuracy of the projection procedure (23) and (24) by analyzing the convergence of the calculated stripping cross sections (22) with respect to n_f. The convergence is illustrated in Fig. 2. From this test one can see that with $n_f=10$ we keep the resulting order of accuracy at the level fixed above—i.e., about 1 % for proton energies greater than 10 keV and somewhat less accurate for lower energies.

Note that with $N=121$, used in our computations, all possible $(l,m)\leqslant(10,10)$ are included completely in the basis (9). This enables us to reach the asymptotic regime [31]

$$\sigma_{ex}(n_i,n_f) \underset{n_f\to\infty}{\sim} \frac{\text{const}}{n_f^3} \tag{25}$$

and thus to make the extrapolation to $n_f\to\infty$, which is important for the excitation as well as for the stripping cross sections $\sigma_{str}(n_i)$.

In Fig. 3 we show the dependence of the calculated excitation cross sections $\sigma_{ex}(n_i=1,n_f)$ on the final n_f. The expected $1/n_f^3$ behavior is rather well attained at $n_f=10$, though not for smaller *n*. This was confirmed by simply fitting a power law between pairs of *n* values. Between $n_f=8$ and $n_f=9$ the power fit is most often between 4 and 5 (there seems to be an anomaly between $n_f=8$ and $n_f=9$ at 0.5 keV in Table II), but between $n_f=9$ and $n_f=10$ the power fit is usually close to 3 (varying between 2.8 and 3.6 for all 38 cases in Tables II–VII). Thus by $n_f=10$ the behavior is quite

TABLE IV. Excitation and deexcitation cross sections $\sigma_{ex}(n_i,n_f)$ for the 2*p* initial state (in units of 10^{-18} cm^2).

E_p	10 keV	100 keV	200 keV	500 keV	1000 keV	2000 keV
$n_f=1$	0.1365	2.681	2.506	1.723	1.143	0.7124
$n_f=3$	166.8	255.8	169.3	84.07	45.79	23.88
$n_f=4$	59.37	47.75	30.07	14.66	8.042	4.251
$n_f=5$	32.29	18.13	11.11	5.338	2.931	1.556
$n_f=6$	19.72	9.077	5.477	2.609	1.431	0.7611
$n_f=7$	13.41	5.266	3.149	1.492	0.8175	0.4350
$n_f=8$	9.351	3.383	2.248	1.063	0.5823	0.3207
$n_f=9$	6.825	2.275	1.347	0.6340	0.3471	0.1848
$n_f=10$	5.039	1.619	0.9557	0.4491	0.2457	0.1308
n_f: $11-\infty$	22.80	7.33	4.32	2.03	1.11	0.59

TABLE V. Excitation and deexcitation cross sections $\sigma_{ex}(n_i,n_f)$ for the 3*s* initial state (in units of 10^{-18} cm^2).

E_p	10 keV	100 keV	200 keV	500 keV	1000 keV	2000 keV
$n_f=1$	0.01936	0.5767	0.2659	0.09737	0.04658	0.02292
$n_f=2$	73.94	35.77	20.89	9.33	4.87	2.48
$n_f=4$	1387	592.3	349.5	156.3	81.20	41.31
$n_f=5$	415.5	142.4	81.93	36.13	18.68	9.472
$n_f=6$	192.5	58.46	33.40	14.70	7.599	3.853
$n_f=7$	109.9	30.55	17.40	7.653	3.959	2.008
$n_f=8$	74.13	18.73	10.65	4.685	2.424	1.230
$n_f=9$	52.42	11.94	6.774	2.979	1.542	0.783
$n_f=10$	40.03	8.28	4.691	2.063	1.068	0.542
n_f: 11−∞	181.0	37.5	21.2	9.3	4.8	2.5

TABLE VI. Excitation and deexcitation cross sections $\sigma_{ex}(n_i,n_f)$ for the 3*p* initial state (in units of 10^{-18} cm^2).

E_p	10 keV	100 keV	200 keV	500 keV	1000 keV	2000 keV
$n_f=1$	0.03170	0.4887	0.4370	0.2969	0.1948	0.1203
$n_f=2$	89.34	61.37	38.96	18.83	10.16	5.273
$n_f=4$	1366	686.7	413.5	188.0	98.24	50.12
$n_f=5$	420.6	160.1	93.68	41.80	21.70	11.03
$n_f=6$	195.3	64.91	37.63	16.71	8.665	4.401
$n_f=7$	111.0	33.68	19.43	8.611	4.465	2.268
$n_f=8$	71.79	20.57	13.46	5.963	3.092	1.571
$n_f=9$	48.61	13.05	7.496	3.315	1.719	0.8736
$n_f=10$	35.64	9.027	5.177	2.288	1.187	0.6032
n_f: 11−∞	161.3	40.8	23.4	10.4	5.4	2.7

TABLE VII. Excitation and deexcitation cross sections $\sigma_{ex}(n_i,n_f)$ for the 3*d* initial state (in units of 10^{-18} cm^2).

E_p	10 keV	100 keV	200 keV	500 keV	1000 keV	2000 keV
$n_f=1$	0.00674	0.06625	0.03597	0.01457	0.00717	0.00357
$n_f=2$	80.61	152.4	100.6	49.76	27.06	14.09
$n_f=4$	1376	879.2	544.6	253.0	133.3	68.21
$n_f=5$	439.6	194.7	114.9	51.28	26.61	13.52
$n_f=6$	203.3	77.33	44.67	19.64	10.14	5.143
$n_f=7$	113.7	39.68	22.67	9.893	5.096	2.582
$n_f=8$	74.30	24.11	15.63	6.807	3.505	1.775
$n_f=9$	50.85	15.19	8.586	3.721	1.913	0.9688
$n_f=10$	37.46	10.47	5.899	2.552	1.312	0.6644
n_f: 11−∞	169.5	47.4	26.7	11.5	5.9	3.0

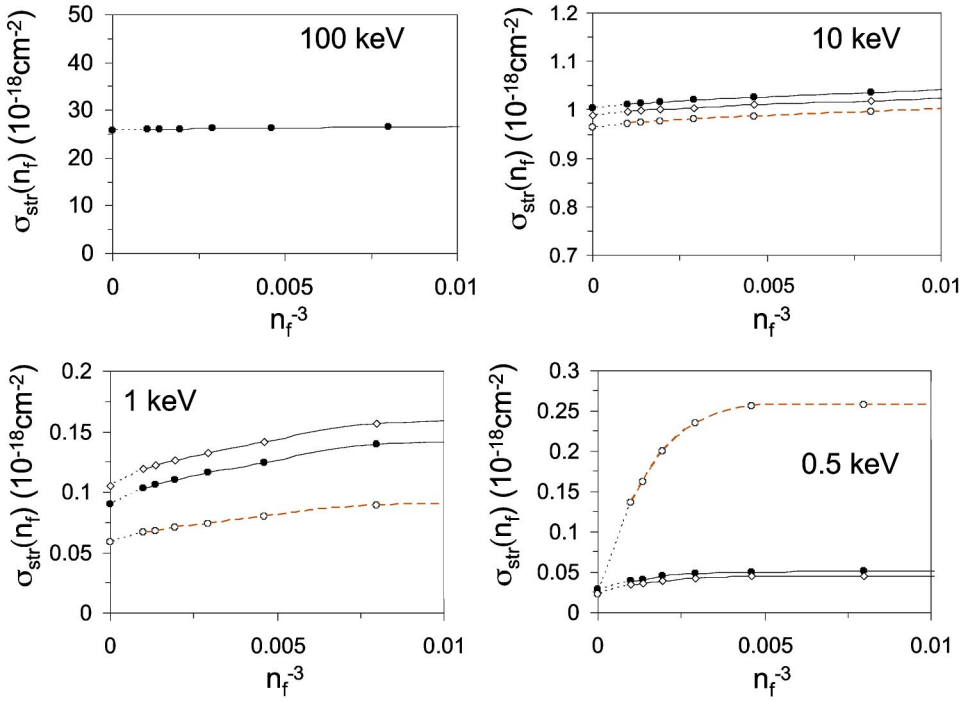

FIG. 4. Extrapolation to the region $n_f \to \infty$ of the calculated cross sections for stripping from $He^+(1s)$ in $p+He^+$ collisions. Curves are denoted as in Fig. 3.

close to the expected asymptotic behavior. This makes the extrapolation very simple; the contribution from $n_f=11-\infty$ is just 4.525 times the cross section for $n_f=10$. This observation enables us to accurately extrapolate the excitation and stripping cross sections to higher n_f. The resulting values are given in Tables I–VII.

The calculations show that the excitation cross sections depend considerably on the trajectory curvature at lower proton energies. Thus the cross sections calculated with a straight-line trajectory differ dramatically at $n_f \geqslant 7$ from the cross sections obtained by direct integration the system of equations (4)–(7). We also show the difference of the strip-

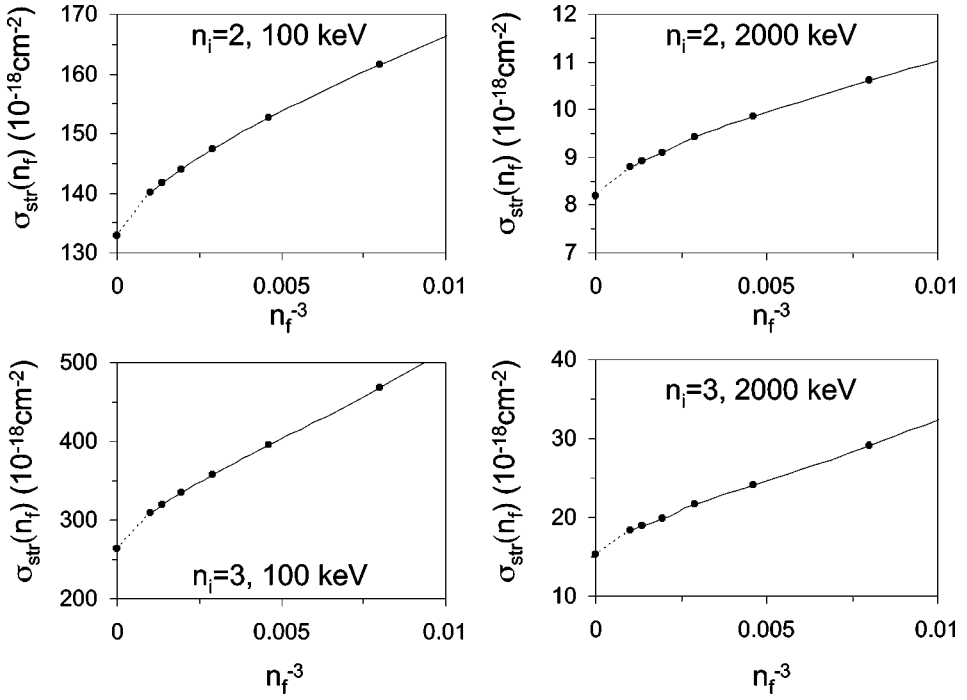

FIG. 5. Extrapolation to the region $n_f \to \infty$ of the calculated cross sections for stripping from the excited states $n_i=2$ and 3 of the $(He^+)_{n_i}$ ion in $p+He^+$ collisions.

ping cross section calculated with a straight-line trajectory at $E_p=0.5$ keV from the result obtained by direct integration of coupled equations (4)–(7). This effect of deformation of the projectile trajectory increases with decreasing collision energy. However, the deviation of the actual trajectory from the Coulomb trajectory is not considerable for $E_p \geqslant 0.5$ keV and has a less important effect on the calculated cross sections. Generally the Coulomb trajectory appears to be the better approximation and should probably be used instead of the more usual straight-line trajectory in a method that requires *a priori* choice of the trajectory (see Figs. 3 and 4).

C. Computations at low collisional energies

Computations at low energies are more challenging in two respects. First, as mentioned above, it is important to include the deformation of the projectile trajectory. Second, the time T must be larger since the distance from projectile to the target before and after collisions, given by $R=\sqrt{(vT)^2+b^2}$, must be similar to make the remaining interaction small. The second effect is illustrated in Fig. 6(b), where a strong dependence on time is seen with decreasing proton energy. Here we may also note the somewhat slower approach to the asymptotic behavior for the stripping cross sections in the case of a straight-line trajectory. This may be understood as due to the projectile leaving the region of interaction faster when trajectory curvature is allowed. In Fig. 6(a) we show the dependence of the calculated cross section on the Z coordinate of the projectile. This analysis showed that for calculations in the region $E_p \geqslant 100$ keV it was sufficient to perform calculations with $T=10$ a.u. in order to obtain 1% accuracy, but for lower energies the integration time must be considerably increased to maintain accuracy.

Another effect that needs to be analyzed for low collision energy is the dependence of the scattering cross sections on the impact parameter b. In Fig. 7 we show the calculated stripping probability $P_{str}(n_i=1,b)$, multiplied by impact parameter b, as a function of b and proton energy E_p. For proton energies above 100 keV—i.e., in the region where ionization dominates (see Fig. 4 of Ref. [32]), the calculated values $bP_{str}(n_i,b)$ have only one maximum, around $b=1$ a.u. At energies below 100 keV, electron transfer becomes dominant in the stripping cross section and leads to the appearance of an oscillating structure in the transition probability $P_{str}(n_i,b)$. These oscillations reflect interference between multiple passes of the electron around the nuclei during the collision (see, e.g., Ref. [6]). Naturally this effect demands more accurate integration over the impact parameter. With increasing collision energy, there is less time for the electron to bounce back and forth between the nuclei, and the oscillations in the transition probabilities are eliminated.

D. Cross sections

In Fig. 8 we present the results of our calculations of the cross sections for stripping from the ground state, as well as the 2*s* and 3*s* states, which are the only excited states that have been previously treated. We also show the results of existing experimental and recent theoretical investigations.

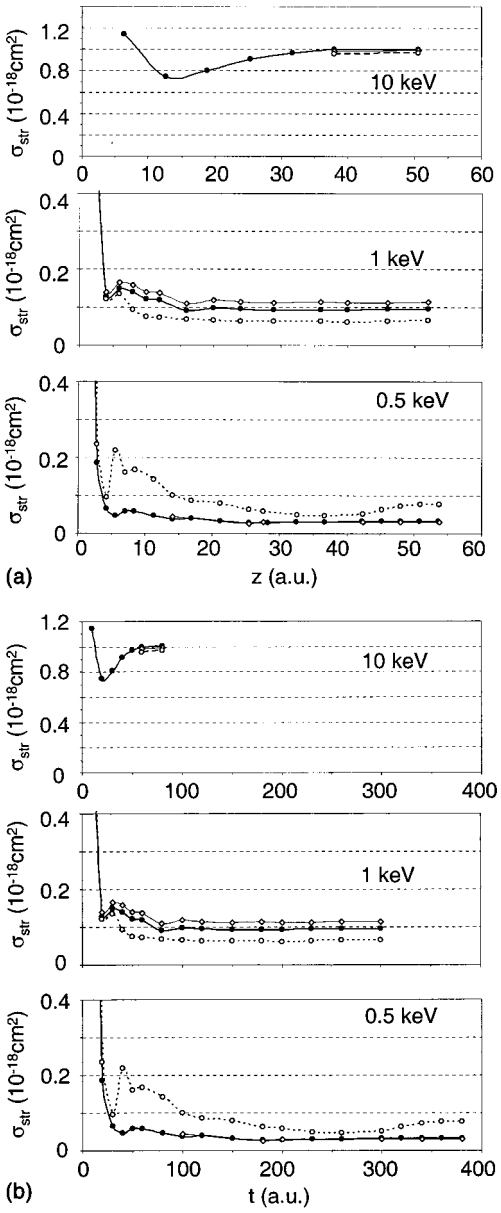

FIG. 6. (a) Dependence of the calculated cross sections for stripping from the ground state $He^+(1s)$ in $p+He^+$ collisions on the Z coordinate between the proton and the ion after the collision. (b) Time evolution of the calculated cross sections for the stripping from $He^+(1s)$ in $p+He^+$ collisions. Solid curves, the results obtained by solving simultaneously the quantum-semiclassical system of equations (4)–(7); thin-solid and dashed curves, the results obtained by solving the Schrödinger equation (4) with Coulomb and straight-line trajectories, respectively.

Here the effect of the trajectory curvature can be seen to be essential at low energies. We obtain rather good agreement with existing experimental data, though unfortunately these data have been obtained so far only for proton energies above 3.7 keV. To understand the enhancement in the stripping cross sections near $E_p=1$ keV and subsequent drop with decreasing proton energy, we made a simple quasiclassical estimate of the turning point for the proton having angular momenta that yield the main contributions to the cross section. These estimates show that at around $E_p=1$ keV the

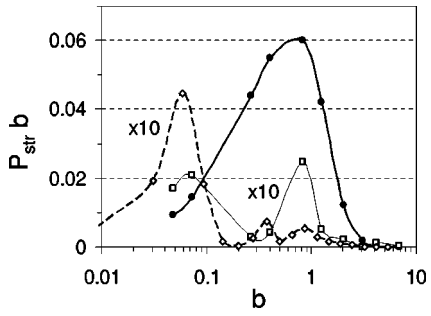

FIG. 7. The probabilities P_{str} [see Eq. (23)], multiplied by impact parameter b, of $He^+(1s)$ stripping in $p+He^+$ collisions as a function of the impact parameter for a few different proton energies. Solid curve, $E_p=200$ keV; thin-solid curve, $E_p=5$ keV; and dashed curve, $E_p=1$ keV. The values are given in atomic units.

classical turning point occurs when the centrifugal potential and Coulomb potential are about equal. With decreasing E_p, the Coulomb potential becomes dominant. This implies more backscattering (with respect to the electron-transfer cross section) and reduces the stripping. Note that previous calculations [7,15] showed faster decay of the electron-transfer cross sections with decreasing energy than found in the present calculations. While we do not have a definitive explanation of this difference, we note that, in the previous close-coupling computations, only a few low molecular states ($n<6$ and $m<4$) were included [15]. However, it is known that with decreasing collision energy the influence of the continuum states can become dramatic, even on the elastic scattering [33]. Also, the importance of interference with the highly excited states at low energies has been noted by

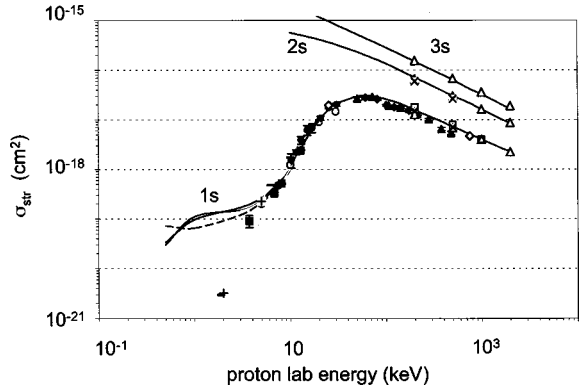

FIG. 8. The cross sections for stripping in collisions between protons and He^+ (1*s*, 2*s*, and 3*s*) ions. Present calculations: solid curves, the result obtained by solving simultaneously the quantum-semiclassical system of equations (4)–(7); thin-solid and dashed curves, the results obtained by solving the Schrödinger equation (4) with fixed Coulomb and straight-line trajectories, respectively. Results of some previous calculations: open triangles, the ionization cross sections of Winter and Winter [3] and Igarashi and Shirai [2] (indistinguishable from each other on this scale); ×, Hall *et al.* [38]; open squares, Errea and Sänchez [39]; open circles, Hose [35]; open diamonds, Stodden *et al.* [40]; solid line, Grozdanov and Solov'ev [7]; +, Winter *et al.* [15]. Experimental results: squares, Peart *et al.* [10]; triangles, Angel *et al.* [11]; circles, Rinn *et al.* [12]; diamonds, Watts *et al.* [13].

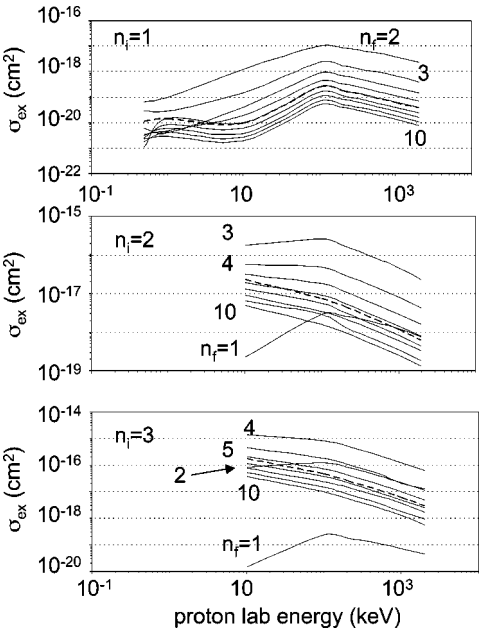

FIG. 9. The excitation and deexcitation cross sections for collisions between protons and $(He^+)_{n_i}$ ions for the transitions from the initial states $n_i=1$, 2, and 3 to the final states n_f. The dashed curve is the extrapolated total cross section for transitions to all excited states with $n_f>10$.

Fritsch and Lin [34]. They, as well as Hose [35], found oscillations at low energies. Our approach correctly includes the effects of both the electronic continuum and interference.

Numerical values of our calculated cross sections are given in the Tables I–VII. In Fig. 9 we illustrate the calculated excitation and deexcitation cross sections for the transitions from the states $n_i=1,2$, and 3 of the He^+ ion. All excitation cross sections peak just above $E_p=100$ keV. Except for a region around 1 keV, the excitation cross sections decrease monotonically with increasing n_f. The secondary maximum in the excitation cross sections for $n_f\geqslant 6$ is likely due to the effect of backward elastic scattering on electron transfer around 1 keV. It would be interesting to test this effect by other methods. It could also lead to the presently found enhancement of electron transfer at such low energies.

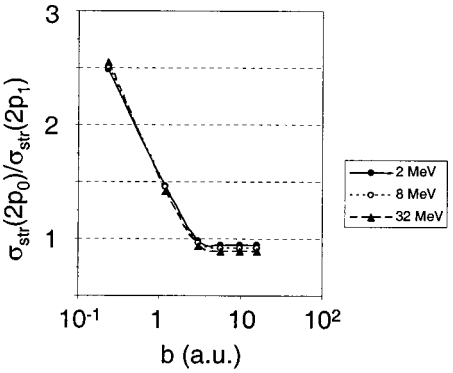

FIG. 10. The ratio of the stripping cross sections $\sigma_{str}(2p_0)/\sigma_{str}(2p_1)$ from the ground state of the He ion as a function of the impact parameter b for three collision energies.

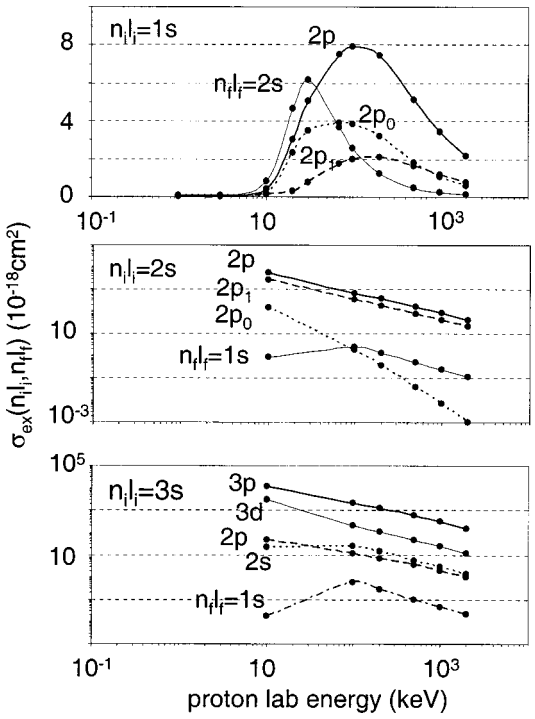

FIG. 11. Some partial excitation and deexcitation cross sections. (a) Dependence of 1*s* excitation cross sections on the quantum number m_f (and their sum), (b) dependence of the 2*s* Stark mixing cross sections on the quantum number m_f (and their sum), and (c) cross sections for 3*s* Stark mixing and deexcitation.

The orientation dependence of these cross sections is usually unimportant in the absence of strong externally applied fields. However, this is not true if something in the application defines a unique axis—e.g., directional detection of the neutron after muon-catalyzed *d-t* fusion in coincidence with detection of the helium ion [36]. In this situation the quantization axis of the helium ion is significant. Thus in Fig. 10 we give the calculated ratio of the stripping cross sections $\sigma_{str}(2p_0)/\sigma_{str}(2p_1)$. At small impact parameters, $\sigma_{str}(2p_0)$ is considerably greater but the two components are similar at large impact parameters. This behavior can be understood in view of the fact that stripping is more probable if the proton projectile is always on the same side of the electron charge density so that the pull is always in the same direction. This is the case if the impact parameter is large compared with the rms size of the helium ion, regardless of the orientation of the orbital. However, in the case of a small impact parameter, the encounter will still be one sided if the charge density is confined to the incident direction (as it is for $2p_0$), but will tend to pass through the center of the charge density if the orientation is perpendicular (as for $2p_{\pm1}$).

Similar considerations apply to the orientation dependence of the excitation and deexcitation cross sections. This dependence is shown for collisions with $He^+(1s)$ and $He^+(2s)$ in Figs. 11(a) and 11(b), whose muonic counterpart is of particular relevance to interpreting some muon-catalyzed *d-t* fusion experiments [36,37]. In the high-energy limit the excitation from a *s* state to a *p* state yields $p_{\pm1}$ but not p_0. The effective high-energy limit depends on the ratio

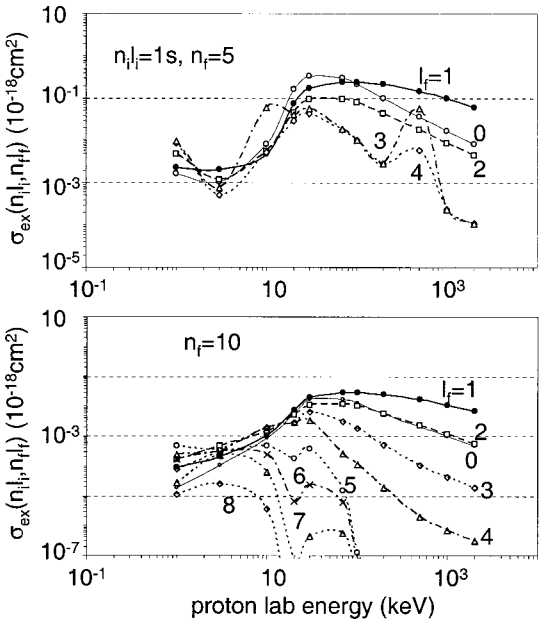

FIG. 12. Partial cross sections for specific final angular momentum (l_f) states (summed over final m_f) in excitation from the ground state to the levels (a) n_f=5 and (b) n_f=10.

of the collision energy to the target splitting, so is achieved at a much lower energy for $2s \rightarrow 2p$ excitation than for $1s \rightarrow 2p$ excitation (even for the former, the effective splitting is nonzero due to the Stark effect).

Of more frequent concern are Stark transitions that take the ion from a metastable (*s*) state to a radiating state. The associated cross sections are shown in Figs. 11(b) and 11(c) for $He^+(2s)$ and $He^+(3s)$, respectively. It can be seen that the

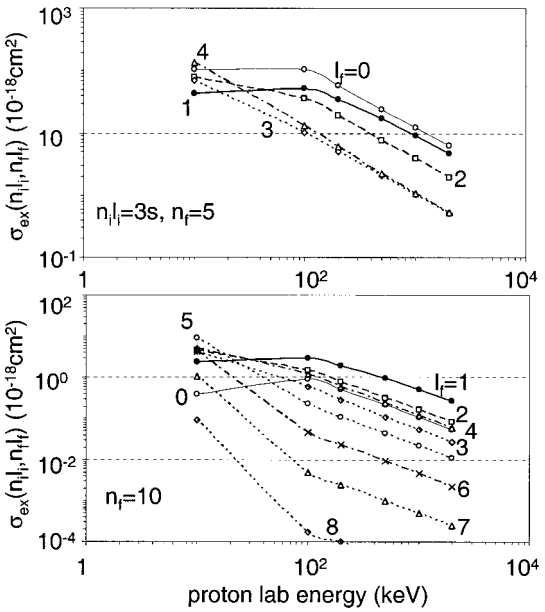

FIG. 13. Partial cross sections for specific final angular momentum (l_f) states (summed over final m_f) in excitation from the 3*s* state to the levels (a) n_f=5 and (b) n_f=10.

Stark transitions generally have larger cross sections than inelastic transitions to lower principal-quantum-number states.

In Figs. 12 and 13 we show how the excitation cross sections depend on the angular momentum of the final state. In the dipole approximation, only $\Delta l = \pm 1$ is allowed, so an *s* state can only go to a *p* state. In most cases this behavior is evident, although it requires going to energies that may be higher than expected. At lower energies it can be seen that the favored state is not always related by this selection rule. The cross sections for excitation to high-angular-momentum states are relatively small and some show anomalous structure. While we believe that the shapes are basically correct, it is true that the accuracy is not as good as it is for small l_f, and we cannot rule out the possibility that this behavior is a numerical artifact.

IV. CONCLUSION

The advantages of the present computational scheme include the following.

(i) The direct numerical calculation of the relative projectile-target trajectory in the simultaneous integration of Eqs. (4)–(7) permits extension of the approach to lower energies where assuming any *a priori* trajectory is unrealistic.

(ii) The algorithm in the present form permits treatment of all the states of the target atomic ion $(He^+)_{n_i}$ up to $n_i = 10$ with accuracies of a few significant digits and enables accurate computations of the stripping and excitation and deexcitation cross sections up to $n_f = 10$.

(iii) We do not use the usual expansion in spherical harmonics and, as a result, avoid the drawbacks of the partial-wave analysis—namely, a multipole expansion of the Coulomb potential (6) and calculation of the resulting matrix elements.

(iv) Applying the special angular and radial grids yields rapid convergence and the possibility to check the accuracy of the computations by employing a sequence of converging grids.

(v) Though not done in the present application, it is also possible in the framework of this approach to consider separately the ionization process (1) by using the technique of projection onto the continuum. In previous work this method was successfully applied to the Coulomb breakup of halo nuclei [22,23]. For that specific problem, it was numerically shown that the procedure is consistent with the alternative technique (22)–(24) of elimination of the bound states from the scattered wave packet.

In summary, we have done calculations at low collision energies where the cross sections are significantly affected by trajectory curvature. Experimental determination at these energies could provide a useful validation of the extended theory.

ACKNOWLEDGMENTS

We gratefully acknowledge valuable discussions with Thomas G. Winter. V.S.M. acknowledges the use of the computing facilities at the Computer Center of the Free University of Brussels. This work was supported by the National Science Foundation through Grant No. Phy-0088936.

[1] H. B. Gilbody, in *Atomic and Plasma-Material Interaction Data for Fusion* [Nucl. Fusion Suppl.3, 55 (1992)].
[2] A. Igarashi and T. Shirai, Phys. Rev. A **51**, 4699 (1995).
[3] T. G. Winter and J. R. Winter, Phys. Rev. A **61**, 052709 (2000).
[4] R. E. Olson, J. Phys. B **11**, L227 (1978).
[5] T. G. Winter, Phys. Rev. A **37**, 4656 (1988).
[6] W. Fritsch and C. D. Lin, Phys. Rep. **202**, 1 (1991).
[7] T. P. Grozdanov and E. A. Solov'ev, Phys. Rev. A **42**, 2703 (1990).
[8] P. S. Krstic and R. K. Janev, Phys. Rev. A **47**, 3894 (1993).
[9] X. M. Tong, D. Kato, T. Watanabe, and S. Ohtani, J. Phys. B **33**, 5585 (2000).
[10] B. Peart, R. Grey, and K. T. Dolder, J. Phys. B **10**, 2675 (1977).
[11] G. C. Angel, K. F. Dunn, E. C. Sewell, and H. B. Gilbody, J. Phys. B **11**, L49 (1978).
[12] K. Rinn, F. Melchert, and E. Salzborn, J. Phys. B **18**, 3783 (1985).
[13] M. F. Watts, K. F. Dunn, and H. B. Gilbody, J. Phys. B **19**, L355 (1986).
[14] T. G. Winter and N. F. Lane, Phys. Rev. A **17**, 66 (1978).
[15] T. G. Winter, G. J. Hatton, and N. F. Lane, Phys. Rev. A **22**, 930 (1980).
[16] V. S. Melezhik, Hyperfine Interact. **101/102**, 365 (1996).
[17] J. S. Cohen, Phys. Rev. Lett. **58**, 1407 (1987).
[18] V. S. Melezhik, Phys. Lett. A **330**, 203 (1997).
[19] V. S. Melezhik, in *Atoms and Molecules in Strong External Fields*, edited by P. Schmelcher and W. Schweizer (Plenum, New York, 1998), p. 89.
[20] V. S. Melezhik and P. Schmelcher, Phys. Rev. A **59**, 4264 (1999).
[21] V. S. Melezhik and P. Schmelcher, Phys. Rev. Lett. **84**, 1870 (2000).
[22] V. S. Melezhik and D. Baye, Phys. Rev. C **59**, 3232 (1999).
[23] V. S. Melezhik and D. Baye, Phys. Rev. C **64**, 054612 (2001).
[24] K. J. McCann and M. R. Flannery, Chem. Phys. Lett. **35**, 124 (1975); J. Chem. Phys. **63**, 4695 (1975).
[25] G. D. Billing, Chem. Phys. **9**, 359 (1975).
[26] N. H. Kwong, J. D. Garcia, and J. S. Cohen, J. Phys. B **22**, L633 (1989).
[27] X. M. Tong, T. Watanabe, D. Kato, and S. Ohtani, Phys. Rev. A **64**, 022711 (2001).
[28] J. V. Lill, G. A. Parker, and J. C. Light, Chem. Phys. Lett. **89**, 483 (1982); J. C. Light and T. Carrington, Jr., Adv. Chem. Phys. **114**, 263 (2000).
[29] D. Baye, J. Phys. B **28**, 4399 (1995).
[30] G. I. Marchuk, *Methods of Numerical Mathematics* (Springer-Verlag, New York, 1975), Sec. 4.3.3.
[31] A. E. Kingston, Phys. Rev. **135**, A1529 (1964).

[32] L. F. Errea, C. Harel, H. Jouin, L. Méndez, B. Pons, and A. Riera, Phys. Rev. A **52**, R2505 (1995).
[33] V. S. Melezhik, L. I. Ponomarev, and M. P. Faifman, Zh. Eksp. Teor. Fiz. **85**, 434 (1983). [Sov. Phys. JETP **58**, 254 (1983)].
[34] W. Fritsch and C. D. Lin, J. Phys. B **15**, 1255 (1982).
[35] G. Hose, Phys. Rev. A **51**, 2222 (1995).
[36] J. S. Cohen and N. T. Padial, Phys. Rev. A **39**, 915 (1989).
[37] H. Bossy *et al.*, Phys. Rev. Lett. **59**, 2864 (1987).
[38] K. A. Hall, J. F. Reading, and A. L. Ford, J. Phys. B **27**, 5257 (1994).
[39] L. F. Errea and P. Sänchez, J. Phys. B **27**, 3677 (1994).
[40] C. D. Stodden, H. J. Monkhorst, K. Szalewicz, and T. G. Winter, Phys. Rev. A **41**, 1281 (1990).